Nuclear Materials and Energy 26 (2021) 100950

Contents lists available at ScienceDirect

Nuclear Materials and Energy

journal homepage: www.elsevier.com/locate/nme

Study of detachment in future ASDEX Upgrade alternative divertor configurations by means of EMC3-EIRENE

T. Lunt [a,*], M. Bernert [a], D. Brida [a], M. Cavedon [a], P. David [a], M. Faitsch [a], Y. Feng [b], M. Griener [a], A. Herrmann [a], B. Kurzan [a], O. Pan [a,c], U. Plank [a], D. Silvagni [a,c], M. Teschke [a], M. Willensdorfer [a], M. Wischmeier [a], E. Wolfrum [a], I. Zammuto [a], the ASDEX Upgrade team [1]

[a] Max Planck Institute for Plasma Physics, Boltzmannstr. 2, 85748 Garching, Germany
[b] Max Planck Institute for Plasma Physics, Wendelsteinstr. 1, 17491 Greifswald, Germany
[c] Physik-Department E28, Technische Universität München, James-Franck-Str. 1, 85748 Garching, Germany

ARTICLE INFO

Keywords:
Power exhaust
Detachment
ASDEX Upgrade
EMC3-EIRENE
Alternative divertor configuration
Snowflake
X-divertor

ABSTRACT

ASDEX Upgrade is preparing a hardware modification of its upper divertor in order to study alternative divertor configurations, like the X-divertor (XD) and the snowflake divertor (SF), that are discussed as a possible solution for the power exhaust problem. Experiments characterizing the current upper divertor in single-null (SN) configuration before and during detachment were carried out recently and interpreted by EMC3-EIRENE (Lunt et al., 2020) now including volumetric recombination. In continuation of these studies we here report on further simulations with this code extrapolating these conditions to the future upper divertor. For the same transport parameters, input power and upstream separatrix density for which the outer target (OT) of the SN is attached, the XD and SF show significant detachment at the OT accompanied by a reduction of the parallel heat flux by a factor of more than five. Despite the shallow field line incidence angles in the XD configuration the intrinsic 3D error fields from the current feeds only cause toroidal variations of the power fluxes of the order of 10%. With a hypothetical misalignment of the divertor coils by 3 cm substantial asymmetries in the power deposition profile are found, however, even those vanish when going to detached plasma conditions. In order to fully detach the plasma at the OT in the SF configuration impurities, here in the form of nitrogen, need to be puffed directly into the region of the secondary X-point in the simulation.

1. Introduction & motivation

Divertor configurations alternative to the conventional single-null (SN) geometry are currently discussed as a solution for the power exhaust problem of tokamaks. For this reason ASDEX Upgrade (AUG) is preparing a modification of its upper divertor [2,3] to study such configurations experimentally, in particular the X-divertor (XD) [4] and snowflake (SF) divertor [5]. An outstanding feature of AUG is its high heating power ($\gtrsim$ 30 MW in total) compared to its size (R = 1.65 m), which makes it particularly suitable for power exhaust studies. An important question is whether the alternative divertor configurations facilitate the access to the detached divertor regime in which the power is dissipated in the plasma volume before reaching the divertor strike point regions [6]. The initial planning of the future upper divertor was based on simple analytical models and numerical simulations [7] with the 3D plasma and neutral particle transport code EMC3-EIRENE [8] that is flexible in handling topologies different from that of the SN. At that time volumetric recombination was not yet included in the code and its capability to describe the detached divertor regime in AUG not yet proven. This motivated the application of the 2D transport code SOLPS, which could be applied successfully for the (to our knowledge) first time for a SF configuration in 2018 [9] after fulfilling a series of technical constraints. While drifts were neglected at that time, they were fully activated for a SF configuration in a follow-up study in 2020 by SOLPS-ITER [10]. According to SOLPS it was found that both the SF [9] and the XD [11] detach at a lower density and/or impurity seeding rate.

However, an intrinsic feature of the XD configuration is the shallow field line incidence angles at the target. In a tokamak such small angles may be problematic since the target alignment inaccuracies and/or magnetic error fields could have a large effect on local power loads. In fact, due to technical constraints significant error fields produced by the current feeds of the new upper divertor coils in AUG are

* Corresponding author.
E-mail address: tilmann.lunt@ipp.mpg.de (T. Lunt).
[1] See the author list of Ref. [1].

https://doi.org/10.1016/j.nme.2021.100950
Received 23 September 2020; Received in revised form 22 January 2021; Accepted 16 February 2021
Available online 20 February 2021

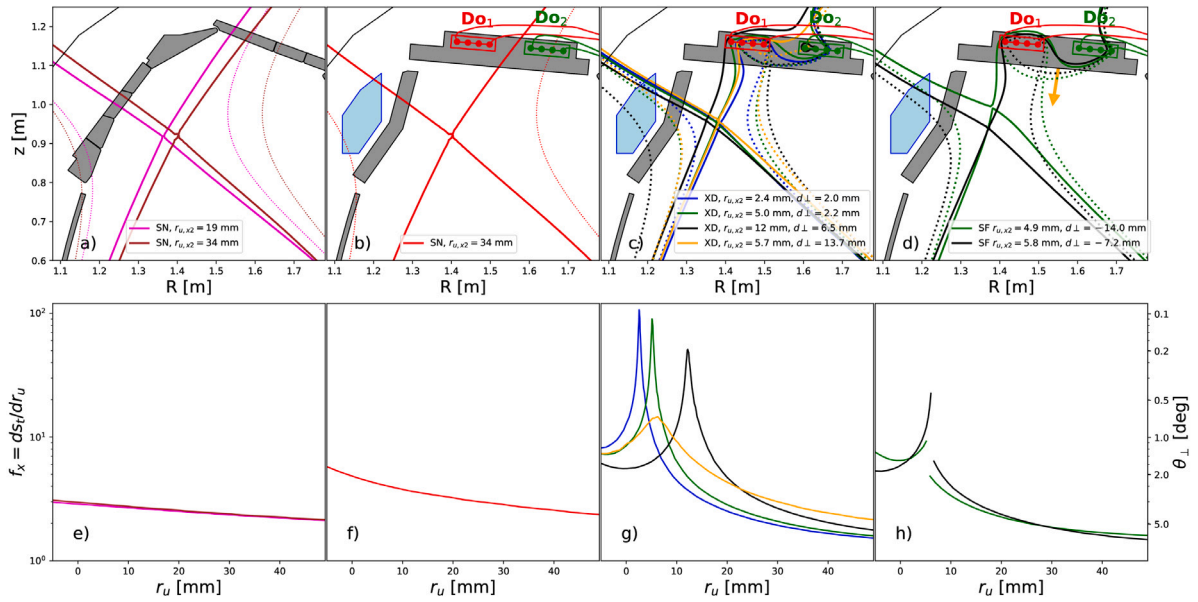

Fig. 1. (a) present geometry of the upper divertor of AUG together with the primary (solid line) and secondary (dotted line) separatrices obtained from the (axi-symmetric) cliste equilibrium reconstruction. The spatial distance of the separatrices at the outboard midplane is given by $r_{u,x2}$. Discharges 35921 at 2.2 s and 36283 at 3.5 s are shown in magenta and brown, respectively. The latter is the reference SN equilibrium that is also shown in (b) together with the future geometry of the planned upper divertor including the upper cryo-pump (blue), the in-vessel coils Do_1 (red) and Do_2 (green) as well as their current feeds. A 3D CAD drawing of that geometry is also shown in Fig. 2. The reference is used for the extrapolation to the alternative configurations in (c) and d), i.e. the X-divertor (XD) and the snowflake divertor (SF), respectively. (e–h) show the flux expansion at the outer target as a function of the upstream coordinate $r_u = R - R_{sep}$ of the equilibria in the row above. (For interpretation of the references to color in this figure legend, the reader is referred to the web version of this article.)

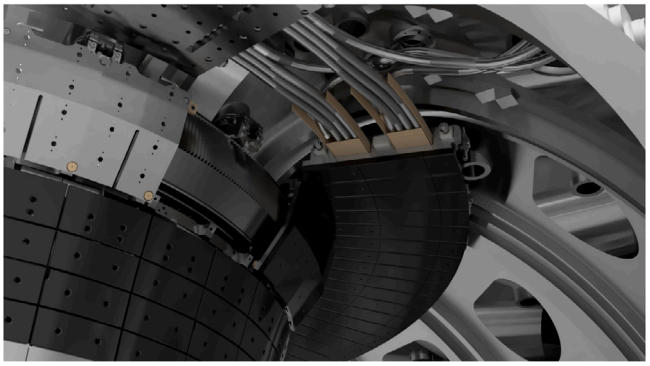

Fig. 2. CAD drawing of the future upper divertor at the position of the current feeds. Some tiles have been removed to see the underlying structure of the conductors. The conductor is guided along a fixed R, z position, i.e. as a perfect circle, along most of the toroidal circumference. Only within the interval $\phi = -90 \ldots -70^o$ it is guided continuously from one turn to another.

unavoidable. Since these fields are 3D the situation was studied with EMC3-EIRENE [11] which showed toroidal asymmetries in the power deposition pattern in particular at high divertor electron temperatures. The simulations showed that the asymmetries become smaller with increasing density, but a prediction for the detached divertor regime could not be made at that time. The question is whether we have to worry about these error fields, if the divertor is strongly detached and the power is dissipated in the plasma volume before hitting the target? Could these error fields cause a 'burn through', i.e. a localized re-attachment of the plasma at a given toroidal position?

Since the last study in 2018/19 the divertor coil geometry was optimized, experiments in upper SN were carried out in AUG to characterize the upper divertor conditions before and during detachment [12] and recombination was implemented in EMC3-EIRENE [13]. With this new version it was recently possible to describe the AUG experiments with a detached upper divertor. Based on this experience we now extrapolate previous studies [11,12] to the new coil and divertor target geometry applying the new code version. Note that Ref. [11] and in particular Ref. [12] are required for the understanding of this work.

2. Geometry & configurations

Fig. 1 a shows the current upper divertor geometry of AUG together with the magnetic equilibria of two USN discharges. Discharge 35921 was already analyzed in Ref. [12]. A particularity of this discharge was the proximity of both the secondary separatrix ($r_{u,x2}$ = 19 mm) and the ICRH limiters ($r_{u,lim}$ = 35 mm) to the primary separatrix at the outboard mid plane (OMP), which lead to a significant power deposition on these limiters in particular at a later phase of the discharge. To avoid this effect here we chose discharge 36283 at 3.5 s as a reference, which has a larger separation of the separatrices ($r_{u,x2}$ = 34 mm) at the OMP and a larger clearance to the ICRH limiters ($r_{u,lim}$ = 53 mm). For the simulations described in the following we otherwise assume the same input parameters including the radial profiles of the cross-field particle and heat diffusion coefficients for electrons and ions $D_\perp$, $\chi_{\perp,e}$ and $\chi_{\perp,i}$ (that are assumed to be constant on flux surfaces, cf. Fig. 3d), the total heating power P_{heat} = 10 MW and separatrix density $n_{e,sep} = 2.1 \cdot 10^{19}\,\mathrm{m}^{-3}$ at the OMP. At this heating power the plasma is clearly in H-mode. The ELMs under these conditions are so frequent that they are barely distinguishable, such that the discharge is in a quasi-continuous exhaust regime [14]. The up- and downstream profiles for these simulations are shown in Fig. 6 of Ref. [12]. The resulting heat flux profile shows different fall-off lengths in the near and in the far-SOL of λ_q^{near} = 3.8 mm and λ_q^{far} = 25 mm, respectively. Power and particle balances are given in Tab. 1 of the same reference. Note that a fixed amount of P_{isb} = 2.3 MW is assumed to be radiated inside the inner simulation boundary and that the total nitrogen impurity radiation $P_{rad,N}$ is kept constant during the iteration process by controlling the integral value of the impurity sources located at the target. This treatment is justified by the experiment that showed that the heat flux profile did not depend on the puffing location and the radiation distribution only very little (cf. the corresponding discussion in Ref. [12]). More details about the (fluid) impurity transport model

can be found in Ref. [8]. Another part of the power $P_{D,SOL}$ and $P_{CX,EL}$ is radiated and transferred to/from the neutral deuterium via charge exchange and elastic collisions, respectively. The neutrals are recycled/reflected at the material surfaces with a probability of one, except for the cold surfaces of the cryo-pump. We come back to the power balances in Sections 3.1, 3.2 and 4.

The magnetic equilibrium of discharge #35921 is also shown in Fig. 1b together with the future divertor geometry including the modified inner and outer targets, the new cryo-pump (blue) and the in-vessel coils Do_1 (red) and Do_2 (green) as well as their current feeds. A 3D CAD picture of the future divertor geometry and in particular that of the conductors is shown in Fig. 2. The fields caused by these conductors are assumed to be given by a sum of the axi-symmetric magnetic equilibrium field and a 3D perturbation. More details about this can be found in Ref. [11]. Driving currents of the order of $|I_{Do1,2}| = 40$ kAt through these coils a secondary X-point (X2) is created close to the target surface, but still outside the plasma (Fig. 1c). The (axisymmetric) magnetic equilibria for these configurations were computed by the Garching equilibrium code [15] assuming the same radial dependence of the toroidal current density j_ϕ. At the target near X2 the flux expansion, i.e. the spatial distance ds_t of neighboring magnetic flux surfaces along the surface compared to their upstream distance dr_u, is very large, as typical for such an 'X-divertor' configuration (cf. Fig. 1g). Note that the flux expansion is inversely proportional to the projected field line incidence angle $\theta_\perp$ (cf. Fig. 2 from Ref. [7]) that is shown on the right scales of Fig. 1e–h. Also note that $\theta_\perp$ can vary toroidally due to the perturbation fields.

Increasing the currents in the coils $Do_{1,2}$ to approximately the maximum nominal value of $|I_{Do1,2}| = 50$ kAt X2 moves into the plasma (cf. Fig. 1d) forming a low-field side snowflake minus (SF) configuration. Note that the term SF is used here for a configuration with a secondary X-point located radially within the power carrying layer of the SOL (i.e. at a distance of the order of the power decay length λ_q upstream) and poloidally between the source position (OMP) and the target. Other authors would call this an 'X-point target' configuration [16]. The configuration analyzed here is rather far away from the original idea of an exact SF that only exists as a mathematical solution and under the assumption of vanishing current density at the X-point [17].

2.1. Reference equilibrium and new target geometry

Before addressing the alternative divertor configurations the effect of the new reference equilibrium and the new target geometry on the SN reference shall be studied alone. Fig. 3 shows the power flux perpendicular to the target $q_\perp$ and parallel to the field lines $q_{||}$ as well as the target electron temperature T_e for different SN configurations. The magenta and brown curves represent equilibria of discharge 35921 at 2.2 s and 36283 at 3.5 s, respectively, but both for the current target geometry (cf. Fig. 1a). The latter has slightly higher power fluxes and target temperatures which are attributed to the larger distance to the ICRH limiters. The smaller impurity source from that limiters is probably also responsible for the slightly lower impurity concentration of $c_{z,lcfs} = 2.6\,\%$ (cf. Fig. 3 brown curves) at the separatrix compared to $c_{z,lcfs} = 3.4\,\%$ (cf. Fig. 3 magenta curves). Quantitatively the effect of the equilibrium is rather small under these conditions (which might not be true for a later phase of the discharge 35921, where the density is higher and a density shoulder [18] has formed).

Due to the need to accommodate the in-vessel conductors, support structures and cooling systems, the outer target (OT) structure is located significantly further downwards and under a different angle compared to the present geometry. For a similar primary X-point position this results in a shortening of the outer divertor leg by approximately 10 cm poloidally (corresponding to a shortening of the field line by about 1.5 m), while the flux expansion is larger by a factor of almost two at the outer strike point (cf. red and magenta colored curves at $r_u = 0$ in Fig. 1e and f). With the same parameters as for discharge

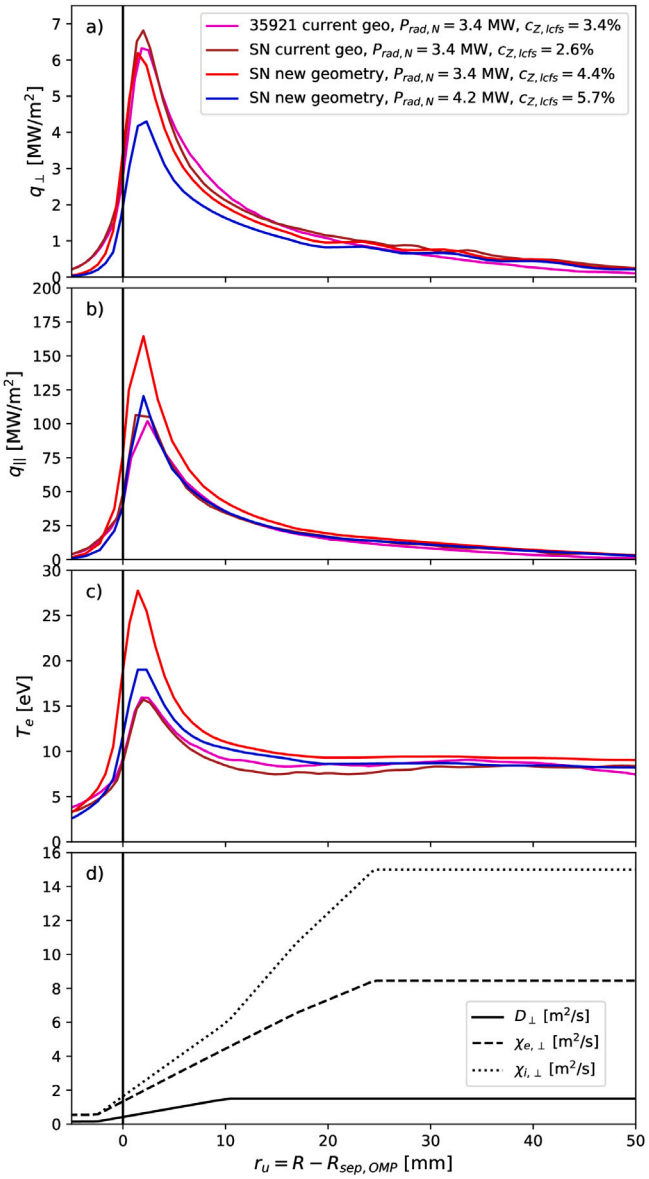

Fig. 3. (a) Power fluxes $q_\perp$ perpendicular to the outer target surface and (b) parallel to the magnetic field lines $q_{||}$ as well as outer target electron temperatures (c) computed by EMC3-EIRENE. The cross-field particle and heat diffusion coefficients for electrons and ions $D_\perp$, $\chi_{\perp,e}$ and $\chi_{\perp,i}$ shown in plot (d) are the same as those in Ref. [12] that were chosen to match the experimental data. (For interpretation of the references to color in this figure legend, the reader is referred to the web version of this article.)

35921 at 2.2 s (cf. Fig. 6 in Ref. [12]) we repeat the simulation for the new geometry *and* the new reference equilibrium. A very similar power flux $q_\perp$ perpendicular to the target surface is found, while the one parallel to the field lines $q_{||}$ is about 60% higher (cf. red and magenta colored curves in Fig. 3). This increase in $q_{||}$ is accompanied by an increase of the peak T_e at the target from 16 to 27 eV for the new geometry (cf. magenta and red curves in Fig. 3c). The change of the geometry alone thus makes it even harder to detach the OT. Increasing the impurity radiation in this configuration to $P_{rad} = 4.2$ MW the power deposition as well as the impurity concentration at the LCFS, $c_{Z,lcfs} = 5.7\,\%$, are still on a high level.

3. X-divertor

The XD configurations are now analyzed in a very similar way as in Ref. [11] by constructing a 360° computational grid (resolution

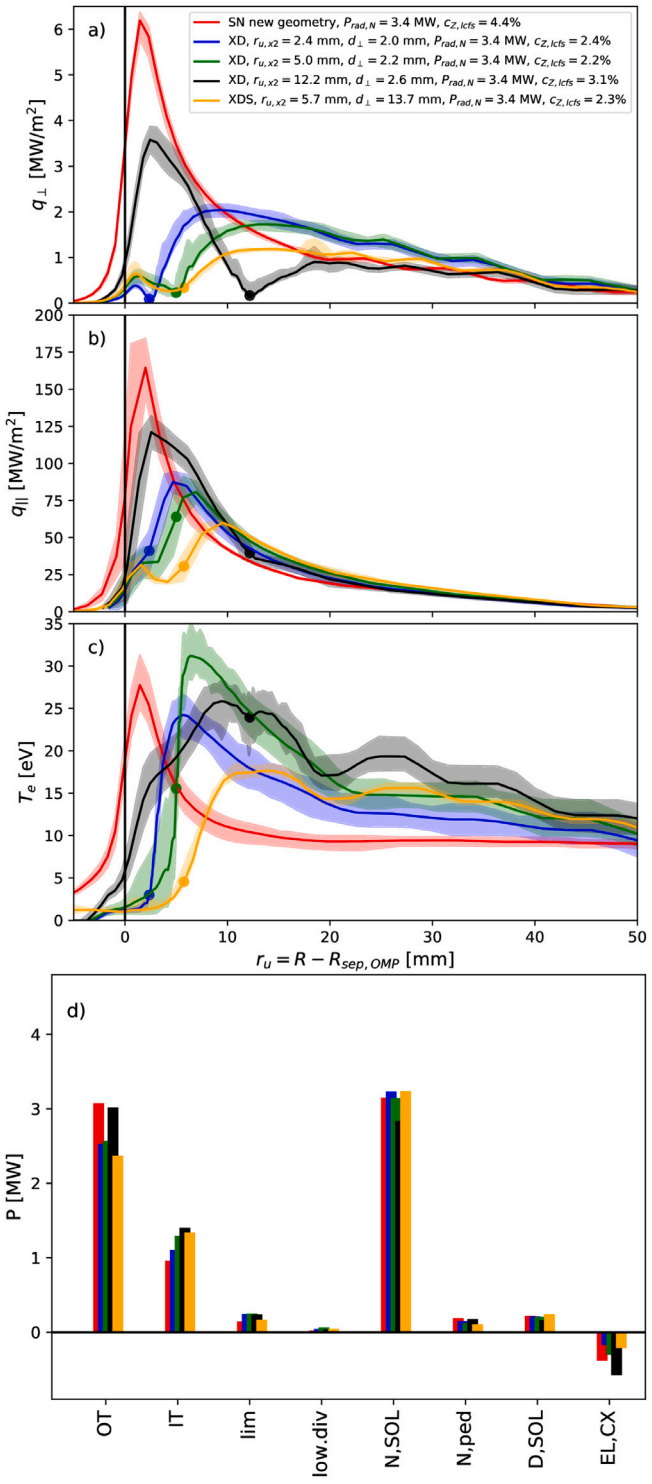

Fig. 4. Radial profiles of (a) power fluxes $q_\perp$ perpendicular to the outer target surface and (b) parallel to the magnetic field lines $q_{||}$ as well as outer target electron temperatures (c) computed by EMC3-EIRENE for a series of XD configurations (cf. Fig. 1b and c) with different separations of the separatrices $r_{u,x2}$ at the outboard midplane. The USN reference discussed in Section 2.1 is shown in red for comparison. In plots (a–c) toroidal variations caused by the 3D error fields from the current feeds are indicated by the areas filled by the same, but fainter colors. The power balances for the same configurations are shown in plot (d) using the same color code.

about 50 × 500 × 270 cells in radial, poloidal and toroidal directions) and including the 3D error fields produced by the current feeds. The currently foreseen geometry of the conductors of the $Do_{1,2}$ coils (cf. Fig. 2) can be regarded as an intermediate case between the previously discussed 'z-joint' and the 'spiral' design (cf. Fig. 7 from Ref. [11]): The conductor is kept at a constant R, z position over a large toroidal interval and guided to the next turn smoothly and without interruption by a joint in the region $\phi = -90\ldots-70°$. We call this design 'S-joggles'. The current feeds are also shown in the poloidal projection of the geometry in Fig. 1b–d. With these error fields, the new code version and the same input parameters as in Ref. [12] similar power deposition profiles as those shown in Fig. 7 from Ref. [11] are computed and compared to the SN reference. In contrast to Fig. 7 from Ref. [11] we here only show the 1D profiles together with the toroidal variation instead of the whole 2D power deposition pattern. Several scans and variations are performed and discussed in the following.

3.1. Scan of the secondary x-point position

The first parameter that is scanned is the radial position of the secondary X-point X2, i.e. the separation $r_{u,x2}$ of the separatrices at the OMP. The poloidal position of X2 is characterized here by its minimum spatial distance $d_\perp$ to the OT surface. Note that due to the proximity of X2 to the in-vessel coils its position can be controlled to a rather high accuracy. Changing the current I_{Do2} from 44 to 45 kAt for example results in a spatial movement of X2 of about 1 cm, which translates into a change of $r_{u,x2}$ of approximately 0.1 mm. The current control accuracy by the power supply is estimated to be of the order of $\Delta I_{Do1,2} = \pm 0.12$ kAt. A similar change of $\Delta r_{u,x2} = 0.1$ mm is caused by a variation of the plasma pressure by 10% (while keeping the plasma current constant), e.g. during an ELM.

Power fluxes for the X2 scan are shown in Fig. 4. Due to the large flux expansion of the XD configurations the power flux $q_\perp$ perpendicular to the target surface is substantially reduced (Fig. 4a). The toroidal variations caused by the error fields are indicated by the underlying shaded areas. A significant reduction of the power flux $q_{||}$ parallel to the magnetic field lines is also observed for the cases $r_{u,x2} = 2.4$ and 5.0 mm (blue and green curves) in the near-SOL region (Fig. 4b) while for the case with $r_{u,x2} = 12.2$ mm $q_{||}$ drops back to 80% of the value of the SN reference. At least for AUG this is an optimistic result since it shows that the configuration can likely be controlled with sufficient accuracy.

For this series of simulations the strongest heat flux mitigation is found for the case with $r_{u,x2} = 5.0$ mm. Note that during this scan the total radiation power from nitrogen as an impurity was kept constant by adjusting the global source. It is found that the impurity concentration $c_Z = n_z/n_e$ just inside the last closed flux surface (LCFS) is reduced to 2.1%, i.e. by more than a factor of two with respect to the SN reference ($c_Z = 4.4$ %). Since impurities inside the confinement region can degrade the performance of a fusion reactor this quantity can be regarded as a cost parameter that shall be minimized.

Finally, another case with a similar $r_{u,x2} = 5.7$ mm, but a slightly retracted X2 in poloidal direction ($d_\perp = 13.7$ mm) was simulated (cf. orange curve in Fig. 4). Interestingly the peak power flux and target temperature are even smaller compared to the case with $r_{u,x2} = 5.0$ mm $d_\perp = 2.2$ mm. This is explained by the larger far-SOL flux expansion (cf. orange and green curves in Fig. 1g for $r_u \gtrsim 10$ mm).

For all these configurations a power balance is shown in Fig. 4d), resolving the contributions from the total deposited power on the outer (P_{OT}) and inner (P_{IT}) target, the ICRH limiters (P_{lim}) and the lower divertor ($P_{low.div}$). Note that P_{IT} increases when moving from the SN to the XD, but that it is always lower than P_{OT}. The maximum $q_\perp$, $q_{||}$ and T_e values along the IT are also smaller or equal to the OT ones. The aforementioned total nitrogen radiation $P_{rad,N} = P_{N,ped} + P_{N,SOL}$ consists of a contribution from the pedestal region ($P_{N,ped}$), i.e. from the region between the LCFS and the inner simulation boundary, and from the SOL ($P_{N,SOL}$) including both divertor legs, the private flux region

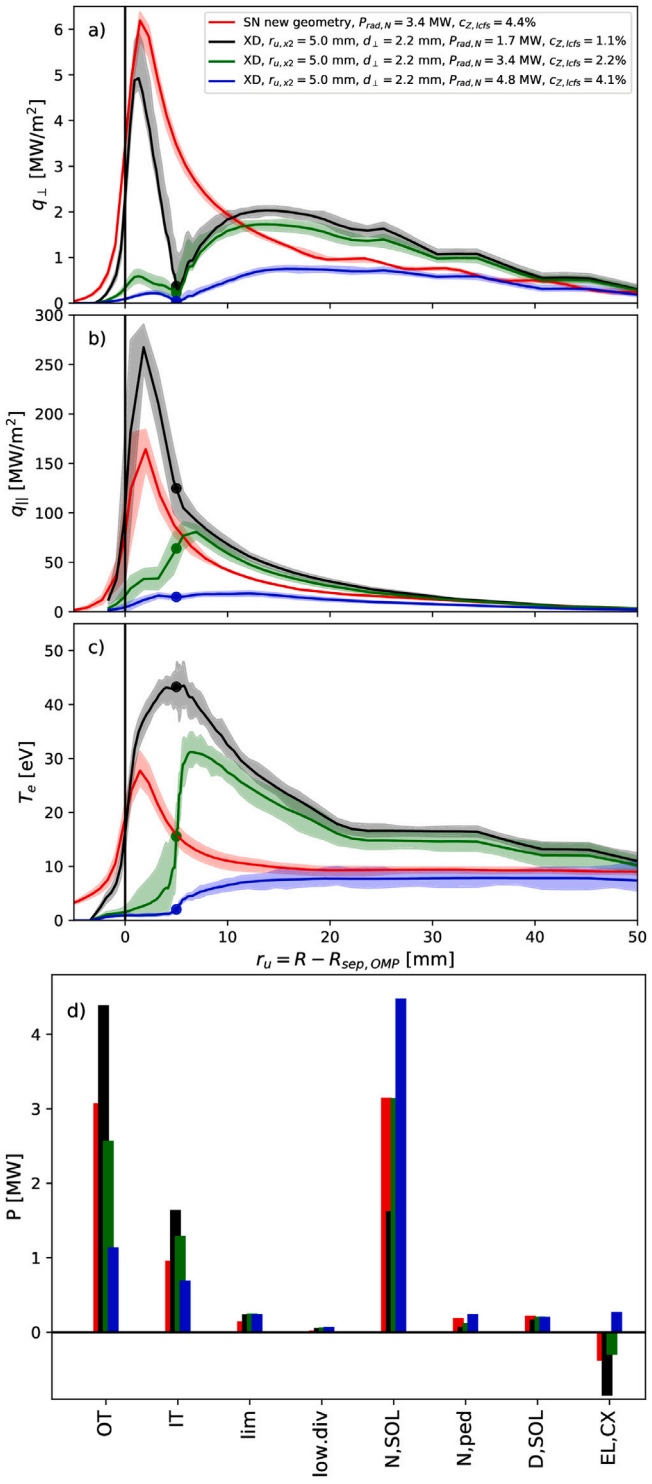

Fig. 5. Same as Fig. 4, but for a fixed magnetic geometry with $r_{u,x2}$ = 5 mm and varying total impurity radiation $P_{N,rad}$. Note that the case with P_{rad} = 4.5 MW (blue curve) still has a smaller impurity concentration $c_{Z,lcfs}$ at the last closed flux surface than the SN reference (red curve).

and regions beyond the secondary separatrix. Deuterium is radiating significantly only in the SOL, $P_{D,SOL}$. Charge exchange and elastic collisions ($P_{CX,EL}$) also contribute to the balance, the contribution can be positive (plasma transfers energy to neutrals) or negative (vice versa). We discuss the negative $P_{CX,EL}$ values observed e.g. for the case with $r_{u,x2}$ = 12.2 mm (black curve) in the next section.

3.2. Radiation scan

For the configuration with $r_{u,x2}$ = 5.0 mm now a radiation scan is discussed. The results are shown in Fig. 5. The scan starts with P_{rad} = 1.7 MW (black curve), i.e. half the value of the SN reference, and is in the attached divertor regime as seen by the electron temperatures at the target above 20 eV in the near-SOL region (cf. black curve in Fig. 5c). It is therefore not surprising that $q_{||}$ is about a factor of two higher at the target (Fig. 5 middle). Due to the large flux expansion, the maximum value of $q_\perp$ (Fig. 5a) is still slightly below the one of the reference. If the error fields caused by the current feeds – and not the mechanical target tile alignment/shaping accuracy – were defining predominantly the toroidal variation of the field line incidence angle at the target surface, this configuration would have a similar peak power load at the target, but a substantially smaller core plasma pollution by impurities ($c_{z,lcfs}$ = 1.1 % compared to $c_{z,lcfs}$ = 4.4 % in the SN reference).

Due to the high electron temperatures ions are accelerated to rather high energies of the order $3T_e$ within the electrostatic sheath in front of the target. Due to the high energy reflection coefficient of tungsten high energetic neutrals are produced there [19] that undergo charge exchange and elastic collisions with the ions of the plasma. If $T_i \sim T_e$ the reflected neutrals can have higher energies than the ions and heat those. For this reason the $P_{CX,el}$ term in the power balance is found to be negative for this case (cf. Fig. 5 d, black curve).

Enhancing the radiation with respect to the original P_{rad} = 3.4 MW (green curves in Figs. 4 and 5) to P_{rad} = 4.8 MW (blue curve) approximately the same impurity concentration $c_{Z,lcfs}$ = 4.0 % than the SN reference $c_{Z,lcfs}$ = 4.4 % is found. This case is then expected to have the same core performance but more than a factor of six lower peak heat flux, both for $q_\perp$ and $q_{||}$. The electron temperature is $\sim$ 1 eV in the near-SOL region indicating detachment. It is below 10 eV along the entire target, which is an important constraint for a reactor that requires a low sputtering yield to guarantee a sufficiently long life time of the divertor.

This also holds for the electron temperature at the IT, although the maximum value is now slightly higher (9 eV) compared to that of the OT.

For this case also a strong drop of the total pressure $p_{tot} = n \cdot \left(T_e + T_i\right)\left(1 + M^2\right)$ between the upstream and the target positions is observed, although this pressure drop is smaller than for the fully detached phase of discharge #35921 (cf. Fig. 7b in Ref. [12]).

3.3. Error fields from misaligned coils

As mentioned in the introduction, an important question is, how sensitive the XD configuration is against toroidal asymmetries of the magnetic field and/or the target geometry. While we already included the 3D error fields of the current feeds at their nominal position in previous sections, here we analyze additional error fields caused by a hypothetical misalignment of the entire coil by dx = 3 cm along the x-axis located at $\phi = 0°$. The engineering tolerance is expected to be smaller than 3 mm, i.e. a factor of ten better, such that this error field can be regarded as an extreme case. At $\phi = 0°$ and $\phi = 180°$ the misalignment is maximum, while it vanishes at $\phi = +90°$ and $\phi = -90°$ such that it is obvious that the resulting error field has a strong $n = 2$ component. Fig. 6 shows the power deposition profile for the same conditions as previous cases with P_{rad} = 1.7 MW (black curves) and P_{rad} = 4.8 MW (blue curves) but including the additional error fields. In the low radiation case the electron temperature in the divertor has strong toroidal variations and can become as large as 50 eV locally (cf. black curves in Fig. 6 bottom). Under these conditions the conductive heat transport becomes very large such that the power deposition footprint is determined to a high degree by the details of these magnetic structures. Toroidal variations of $q_\perp$ ranging from 1 to 9 MW/m^2 are found at the target. Once the divertor becomes colder in the case with

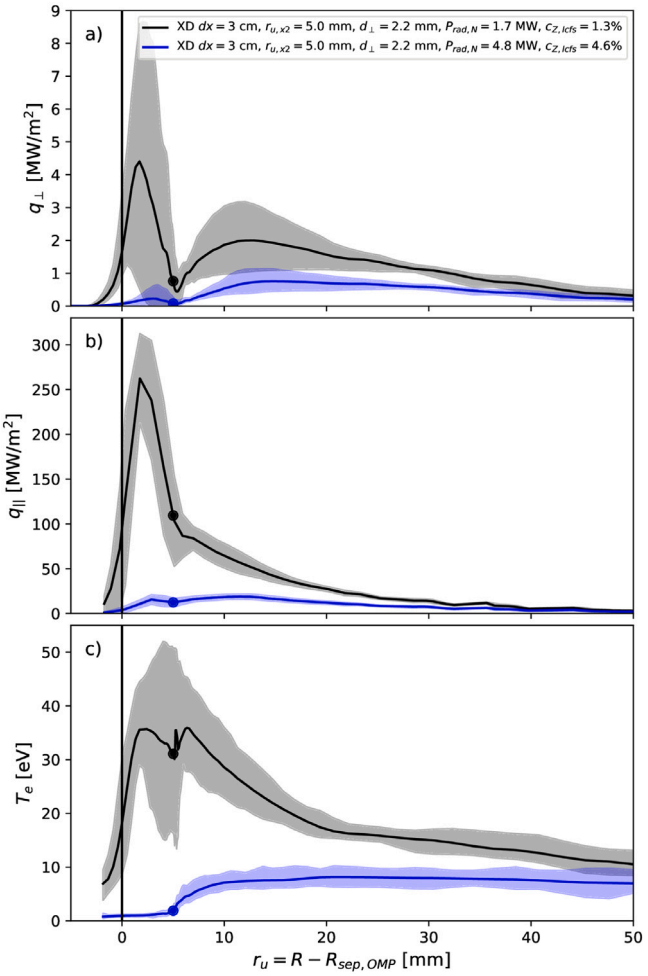

Fig. 6. Same as Fig. 5, but for coils intentionally misaligned by $dx = 3$ cm in direction of the x-coordinate. At low radiation $P_{N,rad} = 1.7$ MW (black curve) $q_\perp$ and T_e very strong toroidal asymmetries of the order of 100%. Increasing the radiation to $P_{N,rad} = 4.5$ MW (blue curve) the outer target detaches and the toroidal asymmetry is substantially reduced, in particular in the near-SOL region. A 'burn through', i.e. a local re-attachment is not observed.

$P_{rad} = 4.8$ MW (blue curves) the parallel transport is substantially reduced and radial transport becomes large enough to smear out these magnetic structures. So the case with $P_{rad} = 4.8$ MW not only has a smaller average power deposition profile but also a substantially lower toroidal asymmetry. This confirms the expectation, formulated already in Ref. [11], that in the detached divertor regime error fields have a by far smaller impact than under attached conditions. It is important to note that despite the presence of the error fields the entire near-SOL region is at electron temperatures of the order of 2 eV. No 'burn-through', i.e. no local re-attachment at a given toroidal position is observed.

Note that all the simulations presented here were carried out assuming Bohm–Chodura boundary conditions at the target, i.e. at the edge of the magnetic pre-sheath [20]. For very shallow field line incidence angles and for high collisionalities deviations from this criterion have been found in particle-in-cell simulations [21].

4. SF-divertor

EMC3-EIRENE simulations with the same input parameters as previously were also carried out for the SF-divertor, but for the time being only for a computational domain with a toroidal extension of $\Delta\phi = 2\pi/16$. The same type of power deposition pattern as for the previous configurations are shown in Fig. 7. Note that the near- and far SOL regions ($r_u \sim 3$ mm and $r_u \sim 10$ mm, respectively) are separated by about 20 cm along the OT (cf. Fig. 1d). The flux expansion is

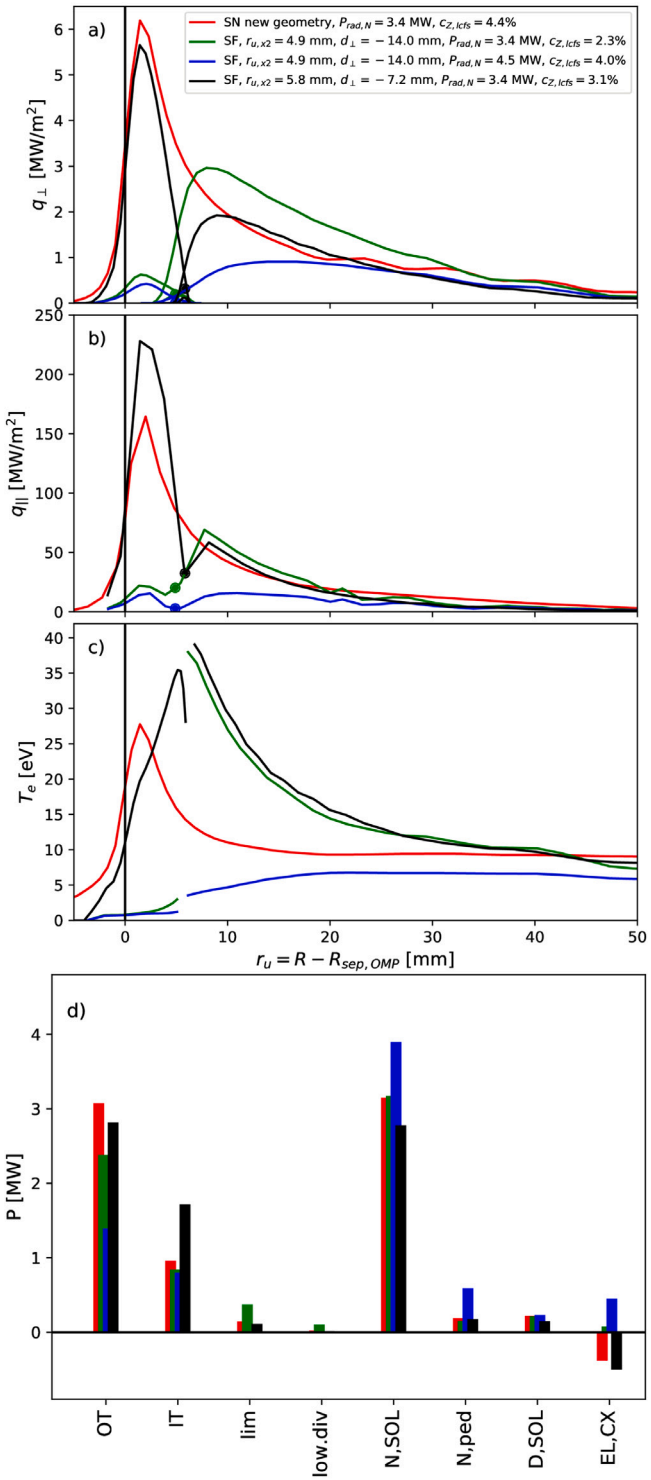

Fig. 7. Same as Fig. 4, but for a snowflake (SF) configuration. The strongest heat flux reduction with impurity sources only at the target is found for $r_{u,x2} = 4.9$ mm (cf. green curve), similar to the X-divertor (XD) configuration. Under these conditions an asymmetry between the primary and the secondary strike points (SPs) are found. Puffing N_2 gas directly into the region of the secondary X-point helps to reduce this asymmetry and to achieve a substantially detached divertor (blue curve). For larger $r_{u,x2} = 5.8$ mm (black curve) a re-attachment of the plasma around the primary strike point is observed.

slightly reduced with respect to the XD configuration as shown by the interrupted curves in Fig. 1 h, but still substantially larger than for the SN. Consequently the projected field line incidence $\theta_\perp$ is larger than for the XD such that the effect of error fields becomes smaller than for the XD.

At first various radial positions of the secondary X-point have been tested keeping the total impurity radiation power at a constant level of $P_{rad} = 3.4$ MW. The one with the strongest heat flux mitigation at the target was the one with $r_{u,x2} = 4.9$ mm, shown by the green curve. For this case a significant asymmetry between the near- and far-SOL fluxes is observed, suggesting that the configuration with the smallest maximum heat flux would be located at a large $r_{u,x2}$. For the configuration with $r_{u,x2} = 5.8$ mm, however, the near-SOL power flux shoots up again indicating a re-attachment of the divertor (where T_e increases to ~ 35 eV). A similar observation was made for a configuration with a smaller $r_{u,x2} = 2.5$ mm (not shown here). The reason for the asymmetry in the case with $r_{u,x2} = 4.9$ mm seems to be the concentration of impurities in the near-SOL region. To counteract this, an additional gas puff location at the OT near the secondary X-point was added in the simulation, while keeping the total nitrogen source at the level required to match the total radiation of $P_{rad} = 4.5$ MW. With this additional source (about 50% of the total) it is finally possible to achieve a far more symmetric power deposition profile with a substantially reduced maximum heat flux compared to the SN reference. Both the near- and the far-SOL regions are now detached.

5. Summary

Alternative divertor configurations are currently discussed as a solution for the power exhaust problem. ASDEX Upgrade (AUG) recently decided the modification of its upper divertor to study such configurations experimentally, in particular the X- and snowflake divertors (XD and SF). The planning of this hardware modification was based on various studies [3,7,9]. An important question is whether alternative divertor configurations (ADCs) can facilitate the access to the detached divertor regime [6], as predicted by recent SOLPS simulations [9]. The 3D transport code EMC3-EIRENE now including volumetric recombination (but not yet drifts) was recently successful in describing the detached upper single-null experiments dedicated to prepare the divertor upgrade [12]. Assuming the same transport coefficients and input parameters as in Ref. [12] the simulations were extrapolated to the situation after the divertor upgrade. In a first step the new outer target (OT) geometry itself was investigated. Due to the shorter poloidal length of the outer divertor leg the target temperature and therefore detachment threshold is higher in the future upper divertor in SN configuration. With currents of the order of 40 kAt in the in-vessel coils a secondary X-point is created inside the OT and the flux expansion is substantially increased, as typical for such an XD configuration. 360° EMC3-EIRENE simulations including the realistic error fields from the current feeds (but no target misalignment) predict a reduction of the power flux $q_\perp$ perpendicular to the OT surface partly due to geometry but also due to a reduction of $q_{||}$. The optimum radial position of the secondary X-point is $r_{u,x2} = 5.0$ mm under these conditions. In the new divertor of AUG, where the coils are close to the secondary X-point, $r_{u,x2}$ is expected to be controllable with millimeter accuracy or better. This configuration with the strongest heat flux mitigation has another advantage namely the lower impurity contamination of the confinement region compared to the SN reference. Increasing the impurity seeding rate up to the point where the impurity concentration reaches the same value as in the SN reference, the plasma at the OT in the XD configuration is fully detached with power fluxes by a factor of more than five smaller than the SN reference. In order to test the sensitivity of the XD configuration with respect to error fields, the coils were misaligned intentionally in the simulation by $dx = 3$ cm, which is by a factor of ten larger than the specified engineering tolerances. For a hot and attached OT these error fields lead to substantial toroidal variations of $q_\perp$ by a factor of almost ten. Once the divertor is detached, however, not only the absolute value of $q_\perp$ drops dramatically, but also its toroidal variation. So even in this extreme case no 'burn through', i.e. no local re-attachment of the plasma is predicted by the simulation.

Finally, the low-field-side snowflake minus (SF) configuration was investigated with the same simulation parameters. A similar optimum $r_{u,x2} = 4.9$ mm as for the XD was found for the SF for the heat flux mitigation at a given total radiation of $P_{rad} = 3.4$ MW. According to simulations with given transport coefficients this value seems to have a narrower tolerance, both increasing or decreasing it leads to a re-attachment of the plasma. Increasing the radiation level globally in the simulation leads to the formation of an asymmetry between the primary and secondary strike points. This asymmetry can however be controlled by puffing the nitrogen impurities directly into the region of the secondary X-point, such that the SF finally also reaches a state of substantial and symmetric detachment. Due to the simplified impurity source/pumping model it is difficult to translate the source strength in the simulation into an impurity injection rate in the experiment. This is left for future work. The possible requirement of an impurity source may be a complication, but it may also be an extra handle to control the power distribution between the primary and secondary strike point. According to our knowledge these are the first EMC3-EIRENE simulations of a detached SF configuration.

CRediT authorship contribution statement

T. Lunt: Carried out EMC3-EIRENE simulations and detailed comparisons with the experimental data. **M. Bernert:** Responsible for bolometry at ASDEX Upgrade and the corresponding tomographic inversions. **D. Brida:** Responsible for the divertor Langmuir probes at ASDEX Upgrade. **M. Cavedon:** Responsible for divertor spectroscopy. **P. David:** Responsible for bolometry at ASDEX Upgrade and the corresponding tomographic inversions. **M. Faitsch:** Responsible for infrared thermography. **Y. Feng:** Main author of EMC3. **M. Griener:** Responsible for the He-beam diagnostics. **A. Herrmann:** Head of the ASDEX Upgrade upper divertor project. **B. Kurzan:** Responsible for the Thomson Scattering system. **O. Pan:** Experienced SOLPS modeler providing valuable discussions concerning the results described in the manuscript. **U. Plank:** Responsible for charge exchange spectroscopy. **D. Silvagni:** Responsible for infrared thermography. **M. Teschke:** Supervision of upper divertor project from electrical engineering side. **M. Willensdorfer:** Responsible for ECE diagnostics. **M. Wischmeier:** Experienced SOLPS modeler providing valuable discussions concerning the results described in the manuscript. **E. Wolfrum:** Supervision of the Li- and He-beams as a senior scientist. **I. Zammuto:** Supervision of upper divertor project from mechanical engineering side.

Declaration of competing interest

The authors declare that they have no known competing financial interests or personal relationships that could have appeared to influence the work reported in this paper.

Acknowledgments

This work has been carried out within the framework of the EUROfusion Consortium and has received funding from the Euratom research and training program 2014–2018 and 2019–2020 under grant agreement No 633053. The views and opinions expressed herein do not necessarily reflect those of the European Commission.

References

[1] H. Meyer, et al., Nucl. Fusion 59 (2019) 112014.
[2] A. Herrmann, et al., Fusion Eng. Des. 123 (2017) 508–512.
[3] A. Herrmann, et al., Fusion Eng. Des. 146 (2019) 920–923.
[4] M. Kotschenreuther, et al., Phys. Plasmas 14 (2007) 072502.
[5] D.D. Ryutov, et al., Phys. Plasmas 14 (2007) 064502.
[6] A. Kallenbach, et al., Nucl. Fusion 55 (2015) 053026.
[7] T. Lunt, et al., Nucl. Mater. Energy 12 (2017) 1037–1042.
[8] Y. Feng, et al., Contrib. Plasma Phys. 44 (1–3) (2004) 57–69.
[9] O. Pan, et al., Plasma Phys. Control. Fusion 60 (2018) 085005.
[10] O. Pan, et al., Plasma Phys. Control. Fusion 62 (2020) 045005.
[11] T. Lunt, et al., Nucl. Mater. Energy 19 (2019) 107–112.
[12] T. Lunt, et al., Plasma Phys. Control. Fusion (2020) http://dx.doi.org/10.1088/1361-6587/aba9ff, in press.
[13] H. Frerichs, et al., Phys. Rev. Lett. 125 (2020) 155001.
[14] M. Faitsch, et al., Nucl. Mater. Energy 26 (2021) 100890.
[15] K. Lackner, Comput. Phys. Comm. 12 (1976) 33–44.
[16] Theiler Ch, et al., Nucl. Fusion 57 (2017) 072008.
[17] P.J. Mc Carthy, et al., 2015 42th EPS Conf. on Plasma Phys. Lisbon, Portugal, June 22–16, P1.188.
[18] D. Carralero, et al., Phys. Rev. Lett. 115 (2014) 215002.
[19] T. Lunt, et al., Plasma Phys. Control. Fusion 59 (2017) 055016.
[20] R. Chodura, Phys. Fluids 25 (1982) 1628.
[21] D. Tskhakaya, Plasma Phys. Control. Fusion 59 (2017) 114001.